Regimes of Coriolis-Centrifugal Convection

Susanne Horn and Jonathan M. Aurnou

Phys. Rev. Lett. **120**, 204502 — Published 15 May 2018

DOI: 10.1103/PhysRevLett.120.204502

Regimes of Coriolis-Centrifugal Convection

Susanne Horn* and Jonathan M. Aurnou
Department of Earth, Planetary, and Space Sciences,
University of California, Los Angeles, CA 90095, USA
(Dated: March 13, 2018)

Centrifugal buoyancy affects all rotating turbulent convection phenomena, but is conventionally ignored in rotating convection studies. Here, we include centrifugal buoyancy to investigate what we call Coriolis-centrifugal convection (C^3), characterizing two so far unexplored regimes, one where the flow is in quasi-cyclostrophic balance (QC regime) and another where the flow is in a triple balance between pressure gradient, Coriolis and centrifugal buoyancy forces (CC regime). The transition to centrifugally dominated dynamics occurs when the Froude number Fr equals the radius-to-height aspect ratio γ. Hence, turbulent convection experiments with small γ may encounter centrifugal effects at lower Fr than traditionally expected. Further, we show analytically that the direct effect of centrifugal buoyancy yields a reduction of the Nusselt number Nu. However, indirectly, it can cause a simultaneous increase of the viscous dissipation and thereby Nu through a change of the flow morphology. These direct and indirect effects yield a net Nu suppression in the CC regime, and a net Nu enhancement in the QC regime. In addition, we demonstrate, that C^3 may provide a simplified, yet self-consistent, model system for tornadoes, hurricanes and typhoons.

PACS numbers: 47.27.te, 47.32.Ef, 47.55.P-

Rotating turbulent thermal convection is the fundamental process underlying a vast variety of geo- and astrophysical flow phenomena, including deep ocean convection, planetary atmospheric flows, and liquid metal core dynamics. Rotating Rayleigh–Bénard convection (RRBC) serves as the paradigm model system; it constitutes a fluid heated from below and cooled from above that is rotated about its vertical axis. Hence, the principal external forces governing the equations of motions are the Coriolis, gravitational and centrifugal buoyancy forces [1, 2]. Traditionally, centrifugal buoyancy is disregarded in RRBC studies [3], based on the claim that it is negligible in natural settings. Exceptions exist but are mainly concerned with the onset properties [2, 4–8, cf. 9], or stably stratified systems [10].

Here, we argue that centrifugal buoyancy warrants inclusion because, like gravity, it drives convective motions: Cold, denser fluid moves radially away from the axis of rotation and warm, less dense fluid moves radially towards it. Further, it breaks the symmetry of the system and thereby changes the range of potential behaviors. Studying Coriolis-centrifugal convection (C^3) - that is RRBC with the full inertial acceleration taken into account - is also exceedingly important for today's state-of-the-art experimental devices that aim to characterize geostrophic turbulence [3, 11]. These experiments must often rotate slower than their actual technical capabilities in order to keep the centrifugal buoyancy small. But it is not known when centrifugal dynamics start to affect important output parameters such as the heat transport and the flow morphologies, nor in which ways those may be altered.

In this Letter, we predict the uncharted regime transitions of C^3 using scaling arguments and provide analytical derivations for the heat transport. Our results are verified and corroborated by direct numerical simulations (DNS), which show a wide range of geophysically interesting flow behaviors.

The governing equations in non-dimensional form are the incompressible Navier–Stokes equations augmented by the temperature equation, viz.

$$D_t\boldsymbol{u} = -\boldsymbol{\nabla}p + \sqrt{\frac{Pr}{Ra\,\gamma^3}}\boldsymbol{\nabla}^2\boldsymbol{u} + \sqrt{\frac{Pr\,\gamma}{Ra\,Ek^2}}\boldsymbol{u}\times\hat{\boldsymbol{e}}_z \quad \text{(1a)}$$
$$+T\,\hat{\boldsymbol{e}}_z - Fr\,T\,r\,\hat{\boldsymbol{e}}_r, \qquad \boldsymbol{\nabla}\cdot\boldsymbol{u} = 0,$$
$$D_tT = \sqrt{\frac{1}{Ra\,Pr\,\gamma^3}}\boldsymbol{\nabla}^2T. \quad \text{(1b)}$$

The temperature T is scaled by the imposed adverse temperature difference Δ; lengths by the radius of the convection vessel R; velocity $\boldsymbol{u}$ by $\sqrt{g\alpha R\Delta}$, where α denotes the isobaric expansion coefficient and g is the gravitational acceleration; time t by $R/\sqrt{g\alpha R\Delta}$ and reduced pressure p by $\rho g\alpha R\Delta$ where ρ is the mean density. The sidewall is insulated, and the top and bottom are isothermal with $T_{top} = -0.5$ and $T_{bot} = 0.5$, respectively. The velocity boundary conditions are no-slip on all walls. The non-dimensional control parameters are the Rayleigh number $Ra = \alpha g\Delta H^3/(\kappa\nu)$, Prandtl number $Pr = \nu/\kappa$, Ekman number $Ek = \nu/(2\Omega H^2)$, Froude number $Fr = \Omega^2 R/g$, and aspect ratio $\gamma = R/H$, where κ is the thermal diffusivity, ν is the kinematic viscosity, Ω the rotation rate, and H is the height of the vessel.

Eqs. (1) are solved numerically in cylindrical coordinates (r, ϕ, z) using the fourth order finite volume code GOLDFISH [12]. In our DNS we can independently vary Fr and the gravitational Rossby number $Ro_\parallel \equiv \sqrt{\frac{Ek^2\,Ra}{Pr}}$ and even set them to 0 or ∞, respectively, while the other remains finite. This numerical flexibility, which is essential to map out the broadest possible parameter space, does not exist in the laboratory, where Fr and $Ro_\parallel$ must co-vary. A total number of 160 DNS are presented

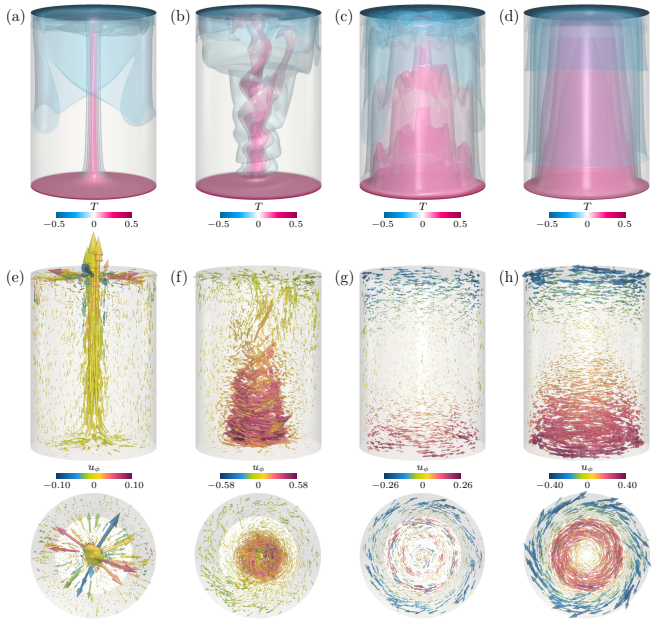

FIG. 1. Flow fields for $Ra = 10^8$, $Pr = 6.52$, $\gamma = 0.365$: (a–d) temperature T, (e–h) side and top view of the velocity vectors scaled in size by velocity magnitude and colored by azimuthal velocity u_ϕ. (a,e) $Ro_\parallel = \infty$, $Fr = 2.0$ (QC); (b,f) $Ro_\parallel = 1.0$, $Fr = 1.0$ (QC); (c,g) $Ro_\parallel = 0.05$, $Fr = 10.0$ (QC/CC); (d,h) $Ro_\parallel = 0.05$, $Fr = 2.0$ (CC). Note that the three rings for (h) at the top and bottom are located at approximately the same radial positions. Corresponding movies can be found in the Supplemental Material.

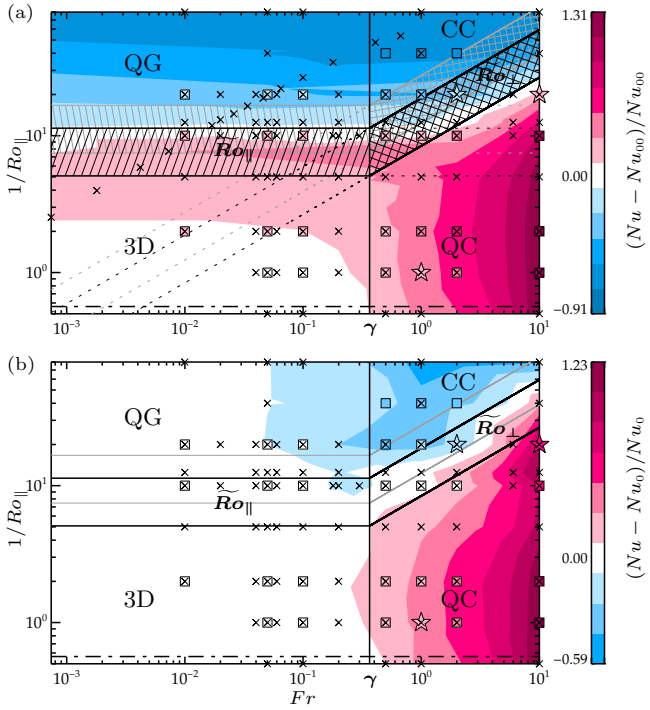

FIG. 2. Relative deviations of Nu from (a) non-rotating, non-centrifugal convection, i.e. with $Fr = Ro_\parallel^{-1} = 0$, and (b) traditional non-centrifugal convection, i.e. with $Fr = 0$. The phase diagrams are based on the DNS conducted at $Ra = 10^7$, the used data points in Fr - $Ro_\parallel^{-1}$ space are marked by crosses. In addition the color-filled symbols show the results for $Ra = 10^8$ using the same color code, where the stars correspond to the cases presented in Fig. 1. The horizontal dash-dotted line indicates the bifurcation $Ro_\parallel$ according to Weiss *et al.* [15]. The black (grey) hatched and cross-hatched area indicate the transition region from the 3D and QC regimes to the QG and CC regimes based on $Ro_\perp$ and $Ro_\parallel$ for $Ra = 10^7$ (10^8). The transition borders are continued with dashed lines. The vertical solid line marks $Fr = \gamma$, the transition from 3D and QG to the centrifugally dominated regimes QC and CC. For clarity, hatching and dashed lines are omitted in (b).

here, conducted with $Pr = 6.52$, $Ra = 10^7$ and 10^8, $0.0125 \leq Ro_\parallel \leq \infty$, $0 \leq Fr \leq 10$ in a cylindrical tank with $\gamma = 0.365$, and a small subset with $\gamma = 1.5$ [13]. Fig. 1 shows characteristic flow fields for the investigated parameter space. (See the movies and Fig. 4 in the Supplemental Material for a broader array of visualizations.)

We first determine when fundamental changes in the dynamics occur in the C^3 system based on time scale arguments. Relevant are the Coriolis time scale, $\tau_\Omega = 1/(2\Omega)$, the gravitational buoyancy (free-fall) time scale, $\tau_{ff} = H/\sqrt{\alpha \Delta g H}$, and the centrifugal buoyancy time scale, $\tau_{cb} = R/\sqrt{\alpha \Delta \Omega^2 R^2}$.

If the flow is three-dimensional (3D), the dynamics happen on time scales $\tau_{ff} \ll \tau_\Omega \ \wedge \ \tau_{ff} \ll \tau_{cb}$. On the other hand, if the flow is quasi-geostrophic (QG), such that the primary force balance is between pressure gradient and Coriolis forces, we have $\tau_\Omega \ll \tau_{ff} \ \wedge \ \tau_\Omega \ll \tau_{cb}$. The ratio of τ_Ω and τ_{ff} yields the gravitational Rossby number

$$Ro_\parallel = \frac{\tau_\Omega}{\tau_{ff}} = \frac{\sqrt{\alpha g \Delta H}}{2\Omega H} = \sqrt{\frac{Ek^2 Ra}{Pr}}, \qquad (2)$$

where $\parallel$ denotes the alignment of the rotation and gravitational buoyancy vectors. We estimate the transition value, $\widetilde{Ro}_\parallel$, from 3D to QG flow using the criterion of King *et al.* [3],

$$6 \lesssim Pr^{3/4} Ra^{1/4} \widetilde{Ro}_\parallel^{3/2} \lesssim 20. \qquad (3)$$

This $\widetilde{Ro}_\parallel$ transition prediction, marked by the hatched area in Fig. 2(a) works well for our Pr and Ra values and is in agreement with other studies [14]. Similarly, if the flow is quasi-cyclostrophic (QC), i.e. the primary force balance is between the pressure gradient and centrifugal buoyancy, the characteristic dynamical scale is $\tau_{cb} \ll \tau_\Omega \ \wedge \ \tau_{cb} \ll \tau_{ff}$. This gives a centrifugal Rossby number [16]

$$Ro_\perp = \frac{\tau_\Omega}{\tau_{cb}} = \frac{\sqrt{\alpha \Delta}}{2} = \sqrt{\frac{Ek^2 Ra Fr}{Pr \gamma}} = Ro_\parallel \sqrt{\frac{Fr}{\gamma}}, \qquad (4)$$

where $\perp$ denotes the perpendicularity of the rotation and centrifugal buoyancy vectors. Based on the similarity of

these two Rossby number definitions, we hypothesize here that the transitional $\widetilde{Ro}_\perp$ also obeys Eq. (3), as indicated by the cross-hatched area in Fig. 2(a).

We predict that the transition to centrifugally dominated flows occurs approximately where the two transition Rossby numbers are equal, corresponding to $\tau_{ff} \simeq \tau_{cb}$ [17]. Crucially, this equivalence occurs at the intersection between the $\widetilde{Ro}_\parallel$ and $\widetilde{Ro}_\perp$ lines in Fig. 2 when

$$\widetilde{Ro}_\parallel \simeq \widetilde{Ro}_\perp \quad \Leftrightarrow \quad Fr \simeq \gamma. \tag{5}$$

Note, that Eq. 5 can be equivalently expressed dimensionally as $H = g/\Omega^2$, and holds irrespective of the specific value of Eq. (3). This regime transition implies, non-intuitively, that centrifugal buoyancy effects will be strongest in low-γ vessels.

For $Fr > \gamma$ there exists an important subregime where $(\tau_{cb} \sim \tau_\Omega) \ll \tau_{ff}$. It is characterized by a triple balance between pressure gradient, Coriolis, and centrifugal force (CC), which is called gradient wind balance [18].

We verify these predictions using the dimensionless heat flux, expressed by the Nusselt number Nu, that has proven to be an excellent tool to indicate regime transitions. The results presented here are for $\gamma = 0.365$; a small set of DNS with $\gamma = 1.5$ is provided in Fig. 5 of the Supplemental Material as supporting evidence. The relative deviation of Nu from the value without rotation $Nu_{00} \equiv Nu(Fr = Ro_\parallel^{-1} = 0)$, is shown in Fig. 2(a). Indeed, $Ro_\parallel$, $Ro_\perp$, and γ adequately describe the borders between different heat transfer regimes [19]. Furthermore, our regime diagram resembles those found in similarly anisotropic geophysical systems (e.g. rotating, stably-stratified dynamics described by Cushman-Roisin and Beckers [20], Fig. 11.6).

For $Fr < \gamma$, the heat transport exhibits the well-known characteristics of Coriolis-affected convection at moderate Pr. With decreasing $Ro_\parallel$ it is initially enhanced due to Ekman pumping in the 3D regime, and then suppressed due to the Taylor Proudman effect in the QG regime [3]. For $Fr > \gamma$, i.e. when centrifugal buoyancy is significant, the two so-far largely unexplored QC and CC regimes show a strong heat transfer increase and decrease, respectively.

Figure 2(b) presents the relative deviation between Nu and $Nu_0 \equiv Nu(Fr = 0)$. The quantity $(Nu - Nu_0)/Nu_0$ differentiates the effects of Coriolis and centrifugal buoyancy forces on the heat transport. Thus, it allows us to visualize the difference in Nu between fully-inertial rotating convection ($Fr \neq 0$, e.g., laboratory experiments) and cases for which centrifugal buoyancy has been omitted ($Fr = 0$, e.g., idealized numerical simulations). The results in Fig. 2(b) confirm the transition prediction (5). Thus, we provide the experimentally testable prediction that a smaller γ value may not necessarily lead to weaker centrifugal effects. This differs substantively from the widespread assumption that centrifugal effects become

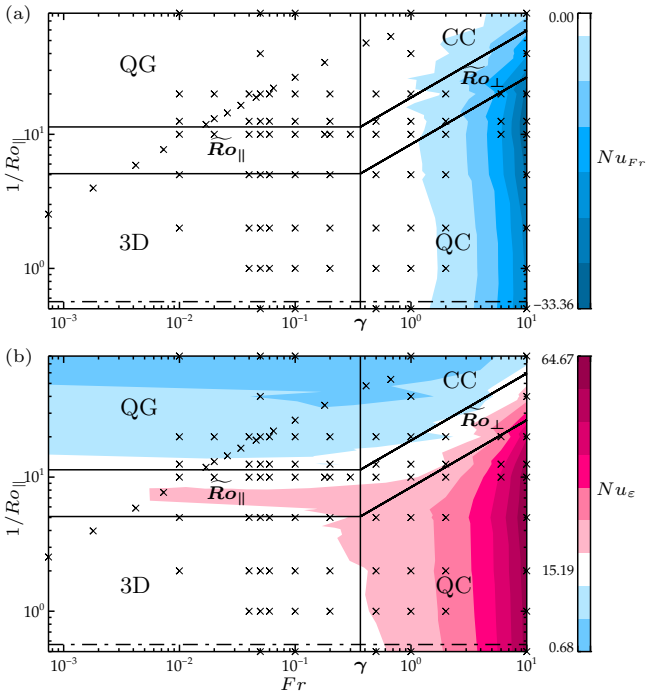

FIG. 3. Nusselt number contributions for $Ra = 10^7$ according to Eq. (6); (a) Nu_{Fr}, (b) Nu_ε. The color scale is calibrated such that white corresponds to the value at $Fr = Ro_\parallel^{-1} = 0$. The lines mark the regime transitions and the crosses mark the Fr and $Ro_\parallel^{-1}$ values of the data points used for the creation of the phase diagram, as in Fig. 2.

important at a fixed estimate of $Fr = 0.05$ [e.g. 3, 7], but instead set in earlier in low-γ vessels. Furthermore, we predict that there is an optimal Ra, according to Eq. (4), along a line of constant $Ro_\perp$ for every experimental setup. Measuring along this line may allow one to map out the heat transport for arbitrary rapid rotation rates with minimal deviations due to centrifugal buoyancy effects.

To explain the contrasting effect of centrifugal buoyancy, we scalarly multiply Eq. (1a) with $\boldsymbol{u}$ and average over the entire fluid volume and time. This yields the exact analytical result

$$Nu = \underbrace{\tfrac{Pr}{\gamma}\langle \|\boldsymbol{\nabla u}\|^2 \rangle_{V,t}}_{\equiv Nu_\varepsilon} + \underbrace{Fr\sqrt{Pr\,Ra\,\gamma}\langle u_r T\, r\rangle_{V,t}}_{\equiv Nu_{Fr}} + 1. \tag{6}$$

For $Fr = 0$, the well-known relationship between heat flux and viscous dissipation rate ε is recovered [e.g. 21]. The extra term Nu_{Fr} in Eq. (6) proves that centrifugation has a direct effect on the heat flux, which is always present. This distinguishes it from pure Coriolis convection. Furthermore, Nu_{Fr} must be negative for sufficiently high Fr, since the hot flow is radially inwards at the bottom, i.e. $u_r < 0$ and $T > 0$, and the cold flow at the top is radially outward, $u_r > 0$ and $T < 0$. This is indeed confirmed by the phase diagram in Fig. 3(a). The main contribution here is stemming from the boundary

layers, where naturally the radial velocities and temperature anomalies are highest.

However, the other term, Nu_ε, counteracts this direct Froude effect. Thus, there is an indirect effect connected to a fundamental change in flow morphology. For $Ra = 10^7$, the maximum positive contribution is almost twice as high in magnitude as the negative effect due to the centrifugality, as shown in Fig. 3(b). The reason for this is the higher ε related to stronger gradients in the velocity field, especially adjacent to the horizontal boundaries.

The flow fields presented in Fig. 1 and in the Supplemental Material elucidate the fundamental changes in flow morphology in the QC and CC regimes. These visualizations show that turbulent C^3 is inherently complex, as it is susceptible to inertial, gravitational, shear, and baroclinic instabilities [4].

The most common behavior of the $Fr \gtrsim \gamma$ flows is a hot central upwelling, and associated with it the known increase of the central temperature [e.g. 9, 22]. This upwelling is visible in all flowfields in Fig. 1 and most prominently in Fig. 1(a,e) for $Ro_\parallel = \infty$ and $Fr = 2.0$. In this case, the primary force balance is cyclostrophic (QC) and the reduced pressure is essentially parabolic in the radial direction. Even with no Coriolis force, symmetry breaking effects suffice to create a retrograde drifting vortex structure in the upper layer with an azimuthal $m = 2$ wave number.

For the other cases $Ro_\parallel$ is finite and the Coriolis force also acts on the fluid, leading to thermal winds. Under the assumption of an axisymmetric, inviscid flow and also neglecting non-linearities and any time-dependence, the C^3 thermal wind balance reads

$$\partial_z u_\phi = Ro_\parallel \gamma^{-\frac{1}{2}} \left(\partial_r T + Fr\, r\, \partial_z T\right). \qquad (7)$$

For $Ro_\parallel = 1.0$ and $Fr = 1.0$ (Fig. 1(b,f)) the primary force balance is cyclostrophic (QC). That is, the pressure gradient and centrifugal forces dominate over the Coriolis force and the strong cyclonic (prograde) wind essentially follows the isobars. As there is a pronounced central pressure minimum where the converging hot fluid rises, the wind has a very small radius of curvature in the lower part of the cell. In addition, the upward flow is helical due to the thermal wind. In the upper part of the cell, where there is a broad pressure high, the flow diverges and becomes more 3D and can even split into two warm streams. Hence, this flow is tornado-like both in appearance and in terms of the underlying physics [23].

When the Coriolis force is stronger, for $Ro_\parallel = 0.05$ and $Fr = 10$ (Fig. 1(c,h); QC/CC), the flow speed goes down and the temperature field is steady and axisymmetric, with a cone-like central hot core. The prograde azimuthal flow is strong in the lower part of the cell and connected to a pressure minimum, so that an eye in the velocity field is formed, where the flow is quiescent. The retrograde circulation at the top is localized to the outer rim.

The last case, shown in Fig. 1 (d,h), for $Ro_\parallel = 0.05$ and $Fr = 2$ is in the triply balanced CC regime. There is a wide pressure high at the top, hence, the flow is anticyclonic (retrograde) and opposed to that is an equally wide pressure low at the bottom where the flow is cyclonic (prograde). This leads to a strong broadening of the temperature distribution compared to the columnar vortices found for lower Fr. Furthermore, concentric ring-like patterns are the prominent flow feature, resulting from centrifugal instabilities [24].

The last two cases demonstrate that QC and CC flows can generate eye- and secondary eyewall-like structures that are qualitatively similar to those found in hurricanes and typhoons [25, 26]and, thus, provide new avenues for the dynamically self-consistent investigation of tornado and tropical cyclone physics.

In sum, our results have substantial implications for the investigation of rotating convection systems. They suggest that the geometry of the tank is crucial to determine the particular regime of Coriolis-centrifugal convection. We make the testable prediction that the transition to centrifugally dominated convection occurs when $Fr \gtrsim \gamma$, instead of a fixed absolute Fr value, as traditionally assumed. In future laboratory and numerical studies, we will further vary γ and make use of other diagnostic tools such as the center temperature [9, 22, but cf. [14]].

* susannehorn@ucla.edu

[1] S. Chandrasekhar, *Hydrodynamic and Hydromagnetic Stability* (Clarendon Press, Oxford, 1961).

[2] F. Marques, I. Mercader, O. Batiste, and J. M. Lopez, J. Fluid Mech. **580**, 303 (2007).

[3] K. Julien, S. Legg, J. McWilliams, and J. Werne, J. Fluid Mech. **322**, 243 (1996); J.-Q. Zhong, R. J. A. M. Stevens, H. J. H. Clercx, R. Verzicco, D. Lohse, and G. Ahlers, Phys. Rev. Lett. **102**, 044502 (2009); R. J. A. M. Stevens, J.-Q. Zhong, H. J. H. Clercx, G. Ahlers, and D. Lohse, *ibid.* **103**, 024503 (2009); E. M. King, S. Stellmach, and J. M. Aurnou, J. Fluid Mech. **691**, 568 (2012); R. P. J. Kunnen, R. J. A. M. Stevens, J. Overkamp, C. Sun, G. F. van Heijst, and H. J. H. Clercx, *ibid.* **688**, 422 (2011); R. E. Ecke and J. J. Niemela, Phys. Rev. Lett. **113**, 114301 (2014); S. Horn and O. Shishkina, J. Fluid Mech. **762**, 232 (2015).

[4] M. A. Torrest and J. L. Hudson, Appl. Sci. Res. **29**, 273 (1974); G. M. Homsy and J. L. Hudson, J. Fluid Mech. **48**, 605 (1971).

[5] J. M. Lopez, A. Rubio, and F. Marques, J. Fluid Mech. **569**, 331 (2006).

[6] J. Lopez and F. Marques, J. Fluid Mech. **628**, 269 (2009).

[7] J. Curbelo, J. M. Lopez, A. M. Mancho, and F. Marques, Phys. Rev. E **89**, 013019 (2014).

[8] N. Becker, J. D. Scheel, M. C. Cross, and G. Ahlers, Phys. Rev. E **73**, 066309 (2006).

[9] J. Hart and D. Ohlsen, Phys. Fluids **11**, 2101 (1999); J. E. Hart, J. Fluid Mech. **403**, 133 (2000).

[10] V. Barcilon and J. Pedlosky, J. Fluid Mech. **29**, 673 (1967); G. M. Homsy and J. L. Hudson, *ibid.* **35**, 33 (1969); N. Brummell, J. E. Hart, and J. M. Lopez, Theoret. Comput. Fluid Dynamics **14**, 39 (2000).

[11] J. S. Cheng, J. M. Aurnou, K. Julien, and R. P. J. Kunnen, arXiv:1703.02895 (2017); J. M. Aurnou, M. A. Calkins, J. S. Cheng, K. Julien, E. M. King, D. Nieves, K. M. Soderlund, and S. Stellmach, Phys. Earth Planet. Inter. **246**, 52 (2015); S. Stellmach, M. Lischper, K. Julien, G. Vasil, J. S. Cheng, A. Ribeiro, E. M. King, and J. M. Aurnou, Phys. Rev. Lett. **113**, 254501 (2014); R. P. J. Kunnen, R. Ostilla-Mónico, E. P. van der Poel, R. Verzicco, and D. Lohse, J. Fluid Mech. **799**, 413 (2016).

[12] O. Shishkina, S. Horn, S. Wagner, and E. S. C. Ching, Phys. Rev. Lett. **114**, 114302 (2015); O. Shishkina and S. Horn, J. Fluid Mech. **790**, R3 (2016).

[13] These parameters are chosen to foster comparison with upcoming experiments using UCLA's NoMag device.

[14] S. Horn and O. Shishkina, Phys. Fluids **26**, 055111 (2014).

[15] S. Weiss, R. J. A. M. Stevens, J.-Q. Zhong, H. J. H. Clercx, D. Lohse, and G. Ahlers, Phys. Rev. Lett. **105**, 224501 (2010).

[16] The square-root of $Ro_\perp$ is also called the density deficit parameter or the thermal Rossby number [9, 10].

[17] This is not expected to be a first order transition, and instead occurs over a relatively broad range centered in the vicinity of $\widetilde{Ro}_\perp \simeq \widetilde{Ro}_\parallel$.

[18] H. E. Willoughby, J. Atmos. Sci. **47**, 265 (1990).

[19] We also indicate where the flow starts to be mildly affected by the Coriolis force according to Weiss *et al.* [15], noting that this holds for almost all of our results.

[20] B. Cushman-Roisin and J.-M. Beckers, *Introduction to geophysical fluid dynamics: physical and numerical aspects*, Vol. 101 (Academic Press, 2011).

[21] B. I. Shraiman and E. D. Siggia, Phys. Rev. A **42**, 3650 (1990); S. Grossmann and D. Lohse, J. Fluid Mech. **407**, 27 (2000).

[22] Y. Liu and R. E. Ecke, Phys. Rev. E **84**, 016311 (2011).

[23] R. Rotunno, Ann. Rev. Fluid Mech. **45** (2013); R. Rotunno, G. H. Bryan, D. S. Nolan, and N. A. Dahl, J. Atmos. Sci. **73**, 3843 (2016); B. H. Fiedler, Quart. J. Roy. Meteor. Soc. **124**, 2377 (1998).

[24] E. L. Koschmieder, Beitr. Phys. Atmos. **40**, 216 (1967).

[25] M. T. Montgomery and R. K. Smith, Annu. Rev. Fluid Mech. **49**, 541 (2017).

[26] S. Nong and K. Emanuel, Q. J. R. Meteorol. Soc. **129**, 3323 (2003).